Experimental assessment of the rotor outlet flow in a twin-entry radial turbine by means of Laser Doppler Anemometry.

José Galindo[1], Andrés Omar Tiseira[1], Luis Miguel García-Cuevas[1] and Nicolás Medina[1]

Abstract

The current paper presents the validation of some hypotheses used for developing a one-dimensional twin-entry turbine model with experimental measurements. A Laser Doppler Anemometry (LDA) technique has been used for measuring the axial Mach number and for counting the number of particles downstream of the rotor outlet. These measurements have been done for different mass flow ratio (*MFR*) and reduced turbocharger speed conditions. The flow coming from each turbine entry does not fully mix with the other within the rotor since, downstream of the rotor, they can still be differentiated. Thus, the hypothesis of studying twin-entry turbines as two separated single-entry turbines in one-dimensional models is corroborated. Moreover, the rotor outlet area corresponding to each flow branch has linear trends with the *MFR* value. Therefore, the rotor outlet effective area used for one-dimensional models should vary linearly with the *MFR* value.

Keywords

Turbocharger, Twin-entry turbine, LDA, Unequal admission conditions, Flow capacity model

[1]CMT – Motores Térmicos. Universitat Politècnica de València, Camino de Vera s/n, Edificio 6D, Valencia 46022, Spain

Corresponding author:
Nicolás Medina, CMT – Motores Térmicos. Universitat Politècnica de València, Camino de Vera s/n, Edificio 6D, Valencia 46022, Spain.
Email: nimeto@mot.upv.es

Introduction

There are several applications for using radial turbines as organic Rankine cycles (ORC), as explained by Yamamoto et al.[1] or distributed generation as microturbines, as described by Facchinetti et al.[2]. However, internal combustion engines (ICE) are its most common application since they are employed in the automotive sector and aircraft powerplants[3].

The increasingly stringent emission standards in ICE in both sectors[4,5] make necessary the development of different techniques to reduce them.

Turbocharging the ICE allows downsizing it and reducing these emissions, as described by Fraser et al.[6]. For engines with multiple cylinders, there are interferences produced by the pulsating flow coming from cylinders of adjacent firing order, as explained by Garrett et al.[7]. These interferences produce many problems as increasing engine back flows or reducing the volumetric efficiency. The solution proposed in Garrett et al.[7] for reducing these interferences is to use multiple-entry turbines, being the twin-entry turbine the solution most usually adopted. Zhu et al.[8] also compared the different turbine configurations coupled with an EGR system obtaining better overall performance with the twin-entry turbine.

However, twin-entry turbines present new issues in the interspace between both volute outlets and the rotor inlet. Aghaali and Hajilouy-Benisi[9] and Brinkert et al.[10] carried out experimental tests for analysing the effect of the different admission conditions. These studies demonstrated the flow admission conditions have a strong effect on the flow behaviour.

Cerdoun and Ghenaiet[11] analysed the interspace between volutes and rotor by means of computational fluid dynamics (CFD) simulations. They found generation of secondary flows with extreme admission conditions in this region. Menaouar et al.[12] proposed to extend the separation wall between volutes with a CFD study. It would reduce the losses produced by secondary flows at extreme admission conditions. However, thermal stress makes it difficult to build. Liu et al.[13] proposed a secondary flow injection system over the shroud section to improve the twin-entry turbine performance. They carried out CFD simulations for optimizing its geometry.

CFD simulations reduce the time and costs in the study of turbochargers. However, they have many sources of uncertainty, as explained by

Cravero and Ottonello[14]. Thus, these simulations must be validated with experimental measurements. Jin et al.[15,16] evaluated the effect of different wastegate and balance valve on twin-entry turbines using both experimental measurements and CFD simulations.

Wei et al.[17] and Xue et al.[18] developed one-dimensional loss-based models for simulating twin-entry turbines. They help to extrapolate and predict twin-entry turbines performance. The authors of this work are also developing a one-dimensional loss-based model described in Galindo et al.[19,20]. It takes into account the losses due to the momentum exchange between flow branches. These losses produce a strong effect on the performance prediction in unequal admission conditions.

This paper aims to corroborate the hypotheses used for developing the one-dimensional model with experimental results obtained with a Laser Doppler Anemometry (LDA) technique.

The LDA technique has been used for many applications as analysing the influence of superheated injection on liquid and gaseous flow field of an experimental single-hole gasoline direct injection injector in Bornschlegel et al.[21] or validating numerical simulations as Kumar et al.[22] for cavitating flow in a multi-hole diesel fuel injector or Theile et al.[23] for the influence of early fuel injection on charge motion in a direct injection spark ignition engine. Grosjean et al.[24] and Fischer[25] studied the suitability of this technique for measuring velocity fields and particles concentration in comparison with other techniques.

This technique has already been employed in turbomachinery. Pedersen et al.[26] studied the flow in a centrifugal pump impeller at design and off-design conditions. Theis et al.[27] analysed the losses in an axial fan with small blade aspect ratios. Zhang et al.[28] measured the unsteady flow fluctuations in a centrifugal pump.

In this paper, the hypotheses used for developing the one-dimensional twin-entry turbine model are corroborated with LDA measurements. Moreover, the CFD simulations used in previous works[19,29] are locally validated in the outlet section with these experimental results. The hypotheses to validate are presented in section Hypotheses to Validate. The experimental setup and the LDA system are described in section Experimental Setup. The test plan is defined in section Test Plan and the results obtained are presented in section Results. Finally, the conclusions are commented in section Conclusions.

Hypotheses to Validate

The twin-entry turbine model previously developed is based on the single-entry turbine model proposed by Serrano et al.[30,31] and Galindo et al.[32] and is detailed in Appendix A: 1D model. The model proposed studies twin-entry turbines as two separated single-entry turbines. This hypothesis is based on the results obtained in Galindo et al.[19].

Steady-state CFD simulations where carried out for different flow admission conditions. The details about these CFD simulations are described in Appendix B: CFD simulations. It was observed that both flow branches did not fully mix within the rotor. Then, the area corresponding to each flow branch at rotor inlet and outlet sections was computed. The CFD results obtained for the rotor outlet section are shown in Fig. 1. These results had linear trends with the *MFR* value. So, another hypothesis used in the effective area one-dimensional model is the linear variation of the rotor outlet area corresponding to each flow branch with the *MFR* value, as shown in Fig. 1.

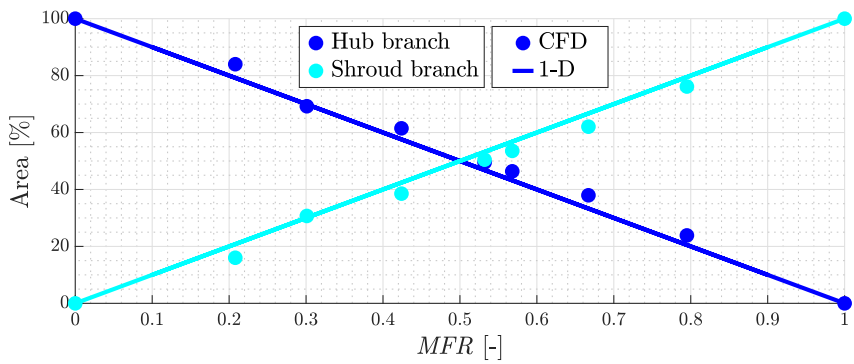

Figure 1. Rotor outlet area obtained from CFD simulations and used for developing the one-dimensional model.

To check if both flow branches does not fully mix within the rotor, an optical technique could be used. Therefore, an optical access to the rotor outlet section is required. Through the optical access, the region where there is flow coming from one of the branches could be captured with an LDA system, differentiating the flow coming from that branch with seed particles.

Moreover, radially distributed measurements are performed to validate the hypothesis of linear area variation.

Experimental Setup

The experimental tests presented in the current paper have been carried out in a gas stand laboratory specially designed for testing turbochargers at different conditions, as explained in Serrano et al.[33].

The turbocharger is independent from the internal combustion engine. Hence, the turbocharger can be measured in both hot and cold conditions. Steady or pulsating flow can also be imposed, as presented in Serrano et al.[34,35]. In the current work, the tests will be carried out with cold, steady flow.

Moreover, the flow admission conditions can be imposed controlling the mass flow passing through each branch. The different flow admission conditions are defined with the Mass Flow Ratio (*MFR*) parameter shown in Eq. 1. This parameter is defined as the ratio between the mass flow passing only through the shroud branch and the total mass flow.

$$MFR = \frac{\dot{m}_{\mathrm{s}}}{\dot{m}_{\mathrm{s}} + \dot{m}_{\mathrm{h}}} \tag{1}$$

In this section, the test bench will be detailed as well as the Laser Doppler Anemometry (LDA) system and the test plan.

Test Bench

The test bench is integrated by four different systems: the compressor, the turbine, the coolant system and the lubrication system. Fig. 2 shows a scheme of the test bench and Table 1 lists the different valves in the test bench for controlling it.

The compressor gets air from the atmosphere. It is operated in an open loop since these work is focused in the turbine flow behaviour. The mass flow passing through the compressor is measured at inlet and outlet sections with thermal mass flow meters. It can be controlled electronically with a back pressure valve, so the working point can be selected from surge to choke conditions. Also, at inlet and outlet compressor sections, the pressure is measured with piezoresistive sensors and the temperature with thermocouples.

The turbine is fed with compressed cold air produced in a two-stage, oil-free, radial compressor. This compressor can provide a maximum pressure of 5 bar, and it is powered by a 450 kW electric motor. There are electronic discharge valves for controlling the pressure and the mass flow

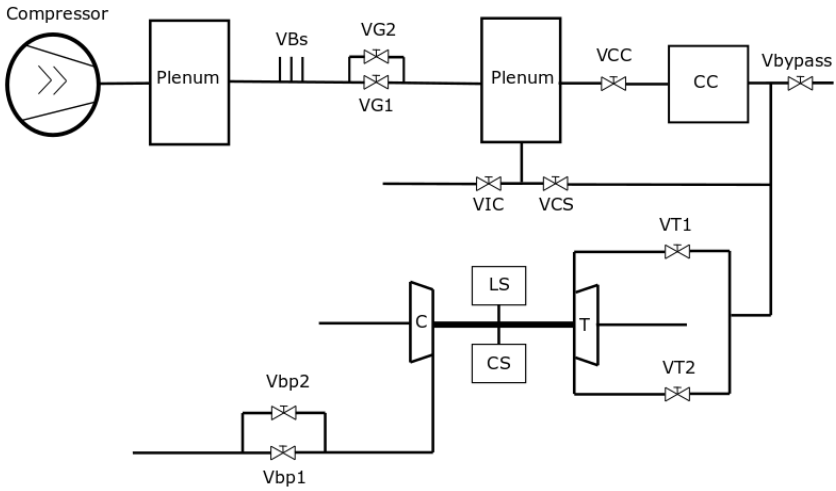

Figure 2. Test bench.

Table 1. List of control valves.

Valve	Action	Symbol
Bleeding valves	Discharge compressed air	VBs
General Valve 1	Control pressure and mass flow	VG1
General Valve 2	Control pressure and mass flow	VG2
Combustion chamber valve	Control hot/cold air	VCC
Cold air valve	Control hot/cold air	VCS
Discharge valve	Discharge compressed air	VIC
Bypass valve	Control combustion chamber outlet	Vbypass
Turbine inlet valve 1	Control flow through inlet 1	VT1
Turbine inlet valve 2	Control flow through inlet 2	VT2
Backpressure valve 1	Control compressor backpressure	Vbp1
Backpressure valve 2	Control compressor backpressure	Vbp2

rate supplied by this compressor. Then, the compressed air is connected to a high-volume plenum for stabilising the flow.

Downstream of this plenum, the air can be heated in a combustion chamber, which can reach temperatures up to 1300 K if hot conditions are required. If cold conditions are required, the plenum can be directly connected to the turbine. The compressed air is split into two independent sets of pipe-work connected with each entry of the twin-entry turbine.

The mass flow is measured with V-cone sensors at both twin-entry turbine inlets and at the turbine outlet. The mass flow of each set of pipe-works is controlled independently with highly linear control valves. The pressure and the temperature are also measured at both inlets and outlet section with piezoresistive sensors and an array of four K-type thermocouples respectively. For measuring the rotational speed of the turbocharger, an inductive sensor is used.

Table 2. Gas stand measurement equipment and precision.

Variable	Sensor Type	Range	Expanded uncertainty
Gas Mass Flow	V-cone, Thermal and Vortex	45-1230 $\mathrm{kg\,h^{-1}}$	≤ 2 %
Gas Pressure	Piezoresistive	0-500 kPa	12.5 hPa
Gas/Metal Temperature	K-type Thermocouple	273-1500 K	1.5 K
Turbocharger Speed	Inductive Sensor	≤ 300 krpm	500 rpm

There is an independent cooling system available for maintaining the temperature constant in sensitive to temperature changes sensors, as the piezoelectric sensors. However, since the measurements in the current tests were performed with cold flow, the coolant system was unused.

There is an independent lubrication system for the turbocharger. It has an electrical heater for controlling the oil temperature and a piloted valve and a recirculation circuit for controlling the oil mass flow. The inlet and outlet temperatures are measured with low uncertainty platinum resistance temperature detectors. The oil mass flow is measured with a Coriolis flow meter.

Finally, the uncertainty of all the turbine measured and computed variables in the test bench is shown in Table 3, computed as described in[36].

Table 3. Uncertainty of the different turbine variables.

Parameter	Average uncertainty	Maximum uncertainty	Units
Temperature	0.47	0.47	K
Mass flow	203	252	mg s^{-1}
Pressure	7.3	7.3	hPa
Rotational speed	500	500	rpm
Reduced speed	3.7	4.7	rpm $K^{0.5}$
Expansion ratio	0.015	0.023	-
Apparent efficiency	0.020	0.049	-
Power	95	216	W
Reduced mass flow	3.45E-8	6.32E-8	m s $K^{0.5}$
MFR	0.0017	0.0054	-

Twin-entry Turbine

The turbocharger used in the current work is a twin-entry turbine with asymmetrical entries and a wastegate. However, the wastegate was completely closed for these tests. The twin-entry turbine used is the one shown in Fig. 3 and its main geometrical parameters are listed in Table 4.

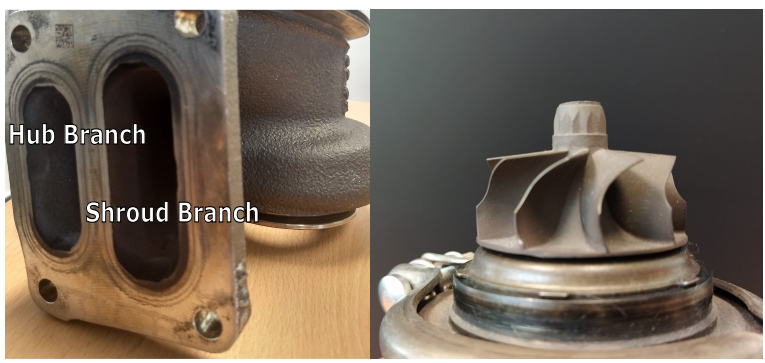

Figure 3. Twin-entry turbine.

Table 4. Twin-entry turbine geometrical parameters and engine parameters on which this turbocharger is used.

Parameter	Value
Rotor inlet diameter [mm]	45.1
Rotor outlet diameter [mm]	40.9
Nut diameter [mm]	12.1
Number of blades	9
Blade inlet height [mm]	6.6
Blade inlet angle [deg]	0
Mean blade outlet angle [deg]	56
Hub branch inlet area [mm^2]	369
Shroud branch inlet area [mm^2]	290
Hub branch A/R [m]	0.0071
Shroud branch A/R [m]	0.0058
Engine type	Gasoline
Number of cylinders	4
Engine displacement [L]	2

LDA system

The LDA system employed is a DANTEC Dynamics system, as shown in Fig. 4a. It does bi-directional measurements with high spatial and temporal resolution. A Bragg cell is used as beam splitter for both directions and the configuration used is back-scatter since it is easier to align. The system has a maximum power of 500 mW per wavelength.

To map the flow field, a traverse system is used for moving the optical head and, so, the intersection volume, as shown in Fig. 4a.

The small particles suspended in the air are injected using the seed particles generator shown in Fig. 4b. It has three valves to control the quantity of particles injected. An oil of refractive index 1.334 and kinematic viscosity 10^{-6} m^2/s is used as seed particles. The particles are injected before the mass flow sensors to take into account the small additional mass flow and to measure correctly the real *MFR* value.

The section of interest for the current work is at the outlet region of the turbine. Therefore, an optical access at this part is required. The turbine outlet case has been machined. Then, a borosilicate glass pipe of the same internal radius as the rotor outlet case has been inserted, as

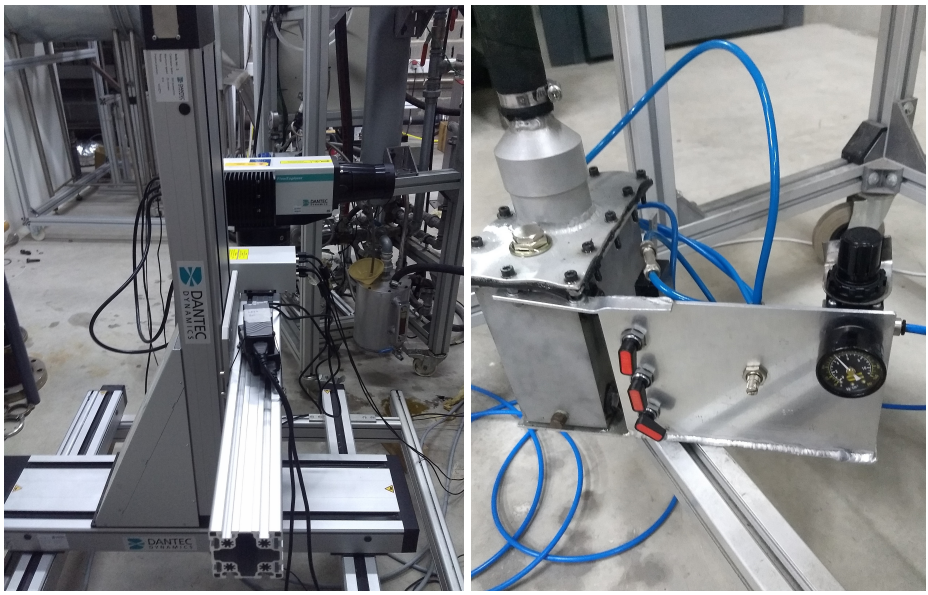

(a) LDA system mounted on a traverse system. **(b)** Seed particles generator.

Figure 4. LDA system.

shown in Fig. 5a. Thus, the laser beams have access to the turbine outlet region as shown in Fig. 5b. Since the pipe is cylindrical, the measurements must be performed at its center for a precise crossing of the laser beams with minimum reflections, avoiding positions very close to the pipe wall. However, it can be properly adjusted with the traverse system.

Test Plan

All measurements carried out are steady-state working points. The primary goal of the current work is to investigate the mixing phenomena of both flow branches. Therefore, unequal admission conditions must be measured. Thus, seven different *MFR* values are measured at three different reduced speeds as listed in Table 5.

Then, six radially separated points are measured with the LDA system for each working point. The radial section measured is 13 mm downstream of the rotor trailing edge. Since the laser beams need separation from all the walls to cross between them, the radial section measured is 3 mm downstream of the rotor nut, as shown in Fig. 5b.

(a) Optical access to the turbine outlet section. **(b)** Laser beams crossing.

Figure 5. Geometry parts that can be differentiated: 1. Volutes, 2. Rotor blades, 3. Rotor nut, 4. Borosilicate glass pipe.

Table 5. Values of *MFR* and reduced turbocharger speed measured.

MFR [-]	N_{red} [rpm $K^{-0.5}$]
0.1	3400
0.2	4000
0.32	4600
0.5	
0.68	
0.8	
0.9	

All the points measured are shown in Fig. 6 in terms of percentage of rotor channel width beginning from hub to shroud. Closer points to the glass pipe wall were unable to capture without noise in the LDA measurements.

Moreover, for each twin-entry turbine working point, the six LDA measurement points are measured twice. The first time the point is measured, the particles are injected through the hub branch. The second time, the particles are injected through the shroud branch. To change the injected branch easily, a valve is placed between the seed particle generator and both sets of pipe-work. Injecting the particles through each branch independently allows to differentiate locally the outlet mass flow corresponding to each twin-entry turbine branch.

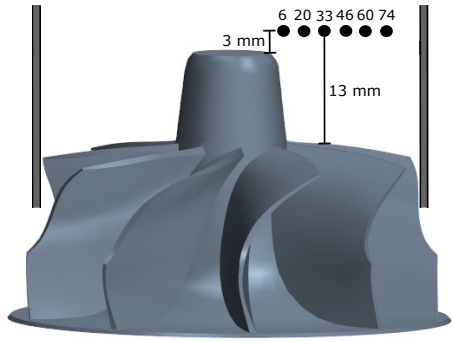

Figure 6. LDA measurements points. The points marked from 6 to 74 are the radial position from hub to shroud in terms of percentage of the rotor channel width.

Results

All steady-state points described in Table 5 are represented in the map shown in Fig. 7. The reduced mass flow is plotted versus the turbine total to static expansion ratio for each twin-entry turbine branch for different MFR and reduced turbocharger speed values. The expanded uncertainty of the reduced mass flow is less than 2 %.

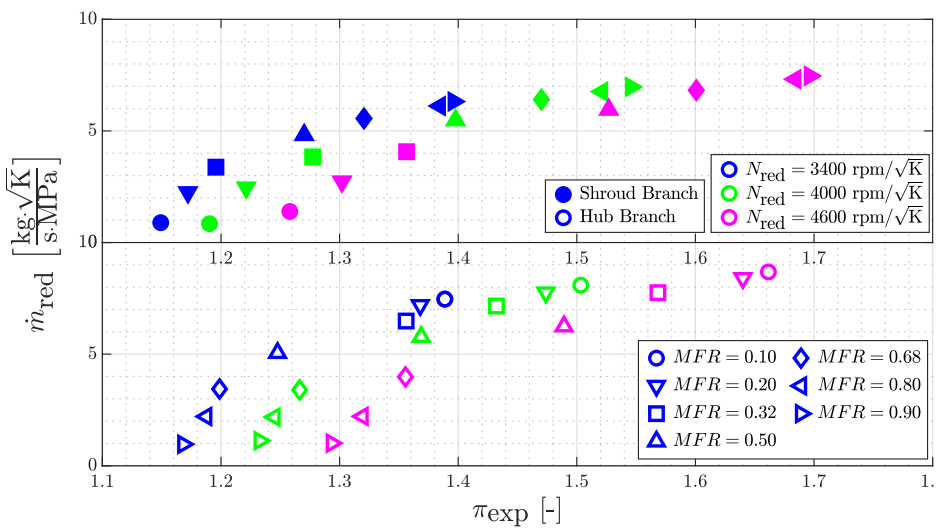

Figure 7. Flow capacity map.

In the current tests, the pressure inlet conditions are increased in order to increase the rotational speed. Thus, higher reduced turbocharger speeds also means increasing the expansion ratio, as seen in the flow capacity map in Fig. 7.

Mach number and rotor outlet flow angle

The axial Mach number, obtained from the axial velocity measured, along the measured points is shown for different MFR values at different rotational speeds in Fig. 8. This figure distinguishes when the oil droplets come from each branch. The empty symbols are the results obtained when the oil is injected through the hub branch. The filled symbols are the results obtained when the oil is injected through the shroud branch. There are measured points that are not plotted, e.g. positions close to hub for *MFR* 0.1 when the oil is injected through the shroud branch. The particles captured in some points were not enough to ensure reasonable statistical results, so they are not included in Fig. 8.

The axial Mach number increases with the rotational speed, since the expansion ratio is also increased. Moreover, the axial Mach number changes along the radial coordinate. It is lower near the nut and higher near the outlet wall. As described in Fig. 6, the LDA measurement points are 3 mm downstream of the rotor nut. There is a sudden expansion just at the rotor nut, as explained in Galindo et al.[20]. This sudden expansion reduces the axial Mach number near the rotor nut, and it explains the axial Mach number distribution along the radial coordinate.

The Mach number plotted in Fig. 8 is the mean value measured. However, it is relevant to know the uncertainty of the measurements. The LDA system provides the root mean square error. Hence, the uncertainty can be calculated following Eq. 2, where RMSE is the root mean square error and n_{samples} is the number of samples captured.

$$u_M = \frac{\text{RMSE}}{\sqrt{n_{\text{samples}}}} \tag{2}$$

Then, this uncertainty can be divided by the mean value to calculate the uncertainty in terms of percentage. Fig. 9 shows a maximum uncertainty of 3% for the axial Mach number. Therefore, it can be assured with a 68% confidence level that the real axial Mach number is the mean value $\pm 3\%$.

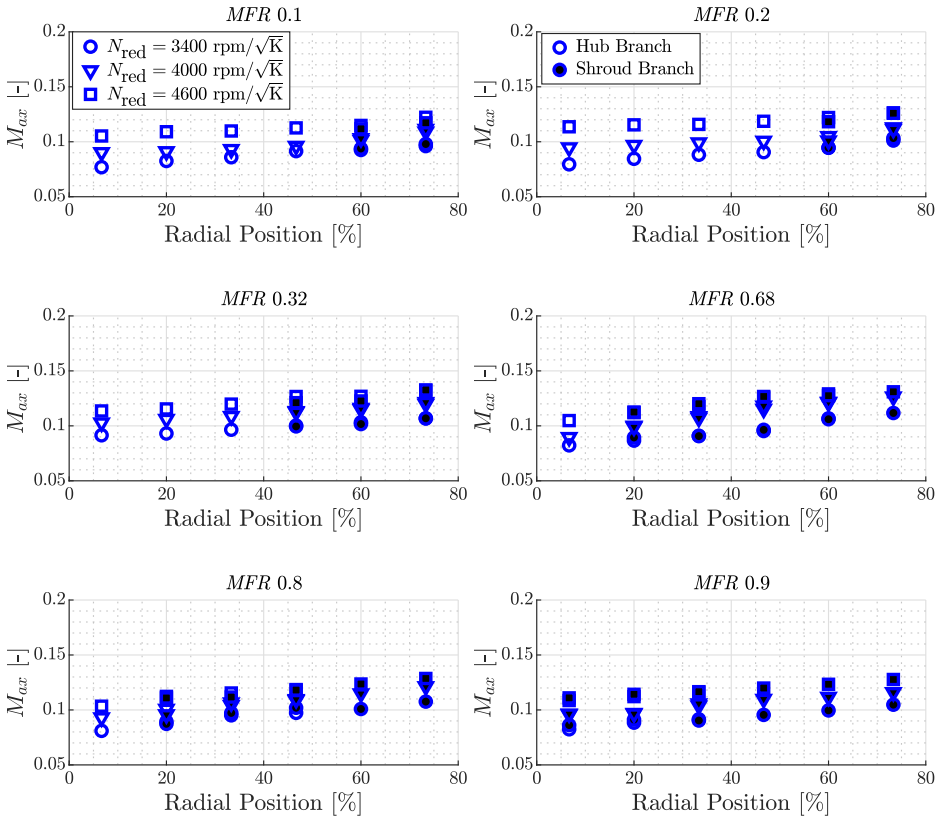

Figure 8. Axial Mach number along the radial position from hub to shroud for different *MFR* and reduced turbocharger speed values. Empty symbols indicate the measurements when the oil is injected through the hub branch and filled symbols when it is injected through the shroud branch.

These measurements can be compared with the results obtained from the CFD simulations at the same section measured with the LDA system. Fig. 10 shows the simulated axial Mach number vs the measured axial Mach number for the hub branch measurements and the shroud branch measurements separately. The dotted lines are the measurements uncertainty. Despite there are some points with higher discrepancies, most of the points are inside the uncertainty range.

Additionally, combining the axial Mach number and the LDA measurements of the tangential component of the velocity for calculating

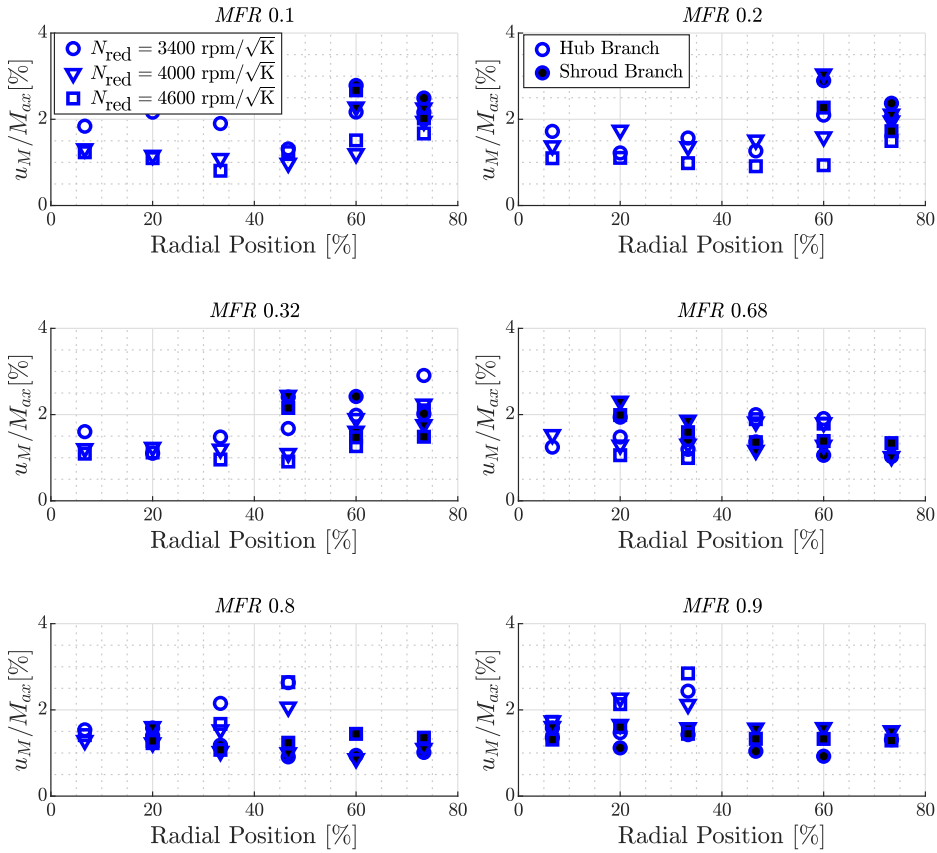

Figure 9. Axial Mach number uncertainty along the radial position from hub to shroud for different *MFR* and reduced turbocharger speed values.

the relative tangential Mach number, the rotor outlet flow angle can be obtained. As indicated in Table 4, the mean blade outlet angle is 56 deg. However, it is not constant along the radius coordinate. The blade outlet angle has values from 44 deg near the hub to 67 deg near the shroud.

Fig. 11 shows the rotor outlet flow angle obtained with the LDA measurements. This angle increases with the radial position as expected, since the blade outlet angle also increases. The reduced turbocharger speed and the *MFR* value have little influence. However, this little influence can be noted particularly in *MFR* values far from full admission condition.

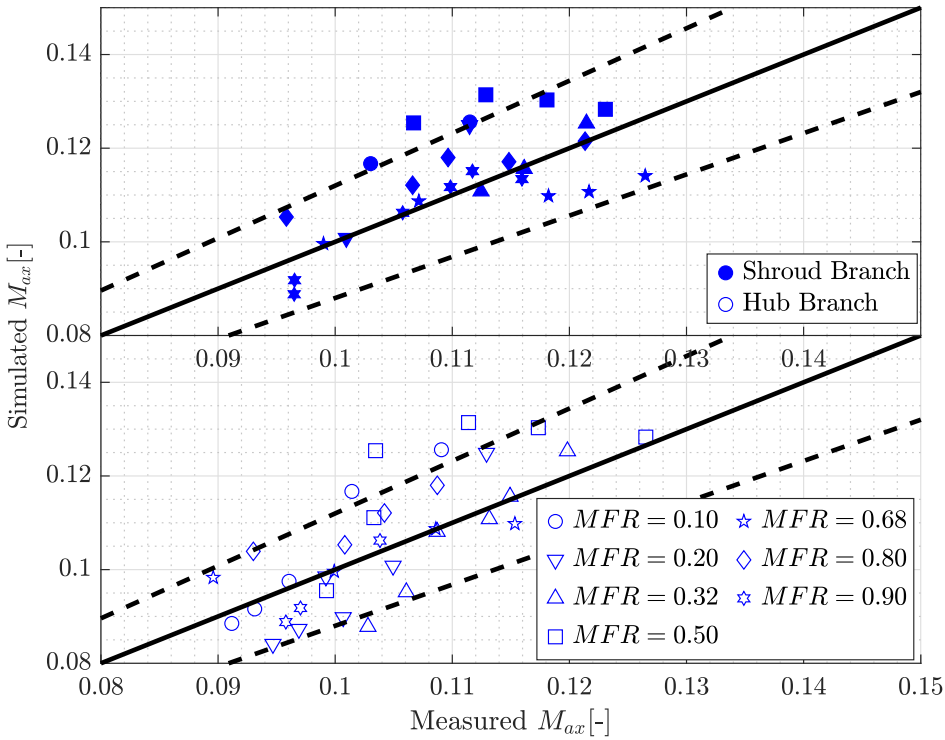

Figure 10. Comparison of the axial Mach number obtained from the CFD simulations and the LDA measurements.

Local concentration

The LDA system measures the velocity locally, but it additionally provides the number of particles captured in the given recording time in that measurement point. As explained in the test plan section, each LDA measurement point is measured twice maintaining the same working point: one injecting the oil through the hub branch and the other injecting the oil through the shroud branch. Since the boundary conditions are the same, the number of particles captured in both measurements can be compared. With this comparison, the proportion of mass flow coming from each branch can be estimated at each LDA measurement point.

To compare the number of particles coming from each branch, the local concentration of particles coming from the shroud branch will be identified with the symbol *SPC*. It is defined in Eq. 3. This value is calculated locally at each LDA measurement point. Thus, the *SPC* can

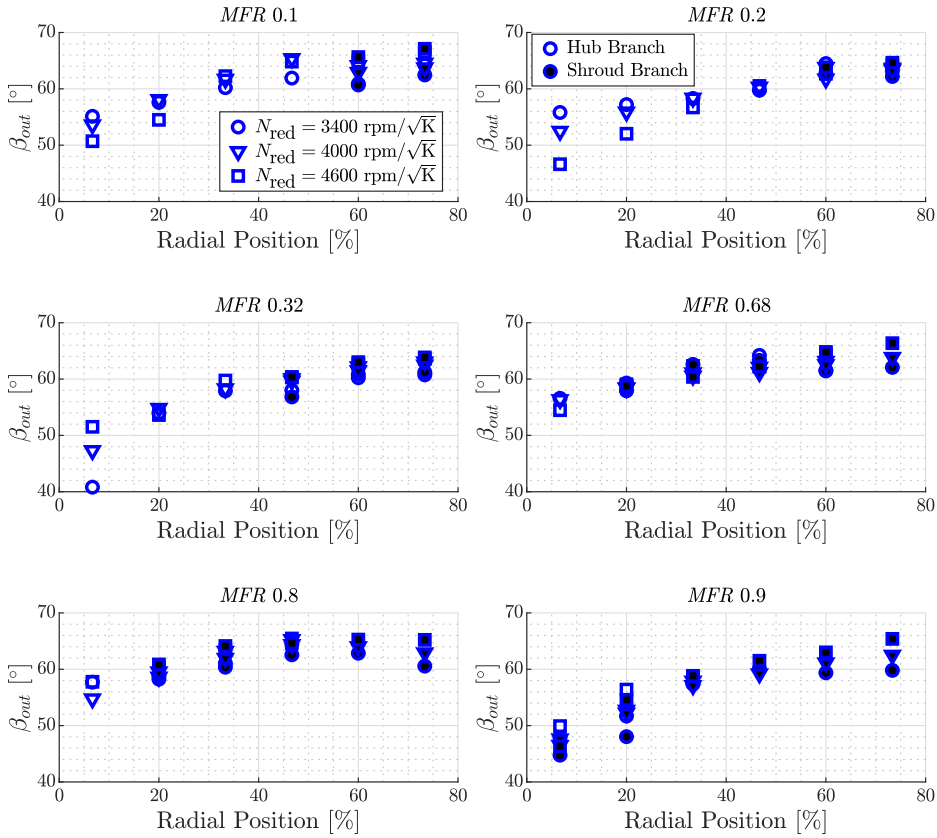

Figure 11. Rotor outlet flow angle along the radial position from hub to shroud for different *MFR* and reduced turbocharger speed values. Empty symbols indicate the measurements when the oil is injected through the hub branch and filled symbols when it is injected through the shroud branch.

be plotted for different *MFR* and reduced turbocharger speed values along the LDA measurement points, as shown in Fig. 12.

$$SPC = \frac{\text{n Shroud Particles}}{\text{n Shroud Particles} + \text{n Hub Particles}} \tag{3}$$

The particle concentration, measured as the particle count coming from one of the branches at a given point divided by the total particle count at that point, is a direct sample of the probability distribution of having flow from that branch instead of flow from the other over the rotor outlet

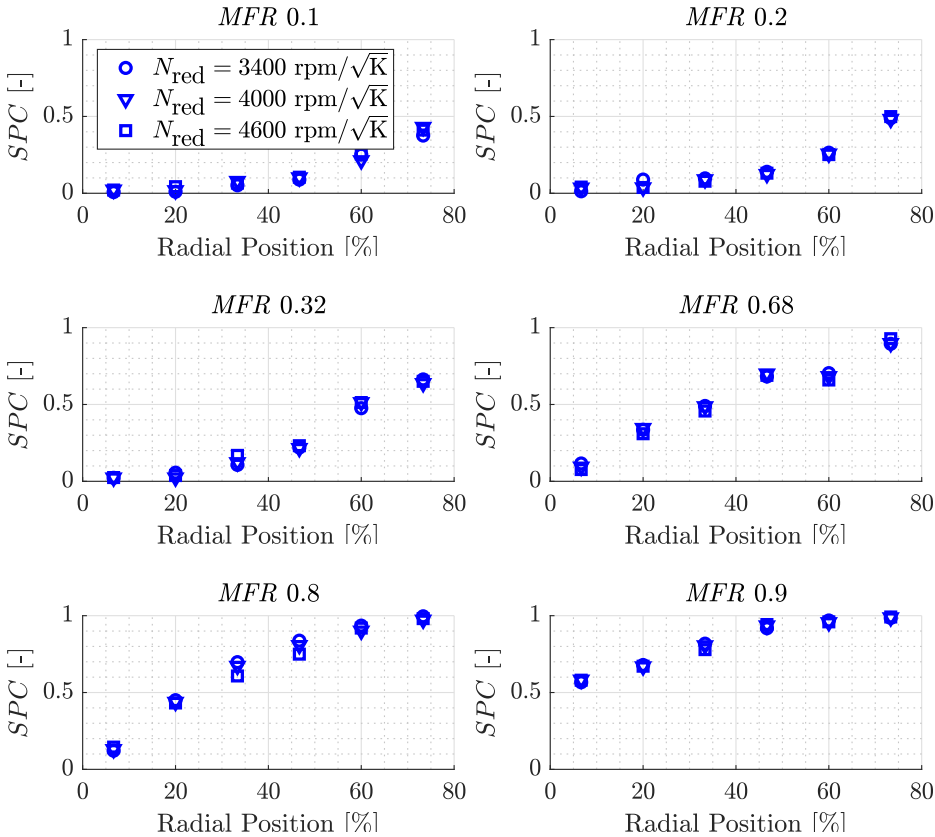

Figure 12. Shroud particle concentration (*SPC*) along the radial position from hub to shroud for different *MFR* and reduced turbocharger speed values.

section. For not-mixed flow, the particle concentration should be either close to 1 if the gas corresponds mainly to the shroud branch, whereas a value close to 0 corresponds to gas coming mainly from the hub branch.

The *SPC* distribution along the LDA measurement points changes with the *MFR* values. However, the reduced turbocharger speed has little influence. When the *MFR* value is increased, the global proportion of mass flow coming from the shroud branch inside the turbine increases. Hence, the proportion of mass flow coming from the shroud branch will be considerably higher in the case of *MFR* 0.9 than in the case of *MFR* 0.1. Fig. 12 shows that the *SPC* increases when the *MFR* value is increased for all LDA measurement points, as it was expected.

However, the *SPC* distribution along the LDA measurement points for the same *MFR* value is not constant. The *SPC* near the rotor hub (positions 0 or 2) is lower than the *SPC* near the glass wall (positions 8 or 10) for all *MFR* values.

In the case of *MFR* 0.1, the global proportion of mass flow coming from the shroud branch is remarkably low and the *SPC* near the rotor hub is nearly zero. In positions closer to the glass wall (positions 8 or 10), the *SPC* is higher. It means the mass flow coming from the shroud branch continues being concentrated near the wall at the outlet region.

In the case of *MFR* 0.9, the global proportion of mass flow coming from the shroud branch is significantly high and the *SPC* near the glass wall is nearly one. In positions closer to the rotor hub, the *SPC* is lower. It means the mass flow coming from the hub branch, continues being concentrated near the rotor hub at the outlet region.

For a more thorough understanding, Fig. 13 shows the *SPC* and axial Mach number results for different *MFR* values and a reduced turbocharger speed of 4000 rpm $K^{-0.5}$. The region plotted comprises only the measured region since there are no data in the middle of the section nor near the pipe wall.

The variation of *SPC* with the *MFR* value is clear, having a higher *SPC* value when the *MFR* increases as expected. In addition, the *SPC* variation along the radial coordinate can be observed. The *SPC* value increases with the radius. It means the flow is not homogeneous at the measured section. Therefore, the flow coming from each entry is not fully mixed with each other in this section downstream of the rotor.

The axial Mach number variation along the radial coordinate can also be observed. There is a Mach number difference of almost 0.1 between the closest point to the centre and the closest point to the pipe wall for this reduced turbocharger speed. As explained in the previous section, the sudden expansion downstream of the rotor nut reduces the axial Mach number near it. Hence, it can explain this axial Mach number variation.

Thus, the mass flow coming from each branch is not fully mixing with the other inside the rotor. The region where there is more mass flow coming from each branch can be differentiated still at the rotor outlet section measured in the current work. So, the hypothesis made in the one-dimensional model [19] of studying twin-entry turbines as two separated single-entry turbines has been corroborated.

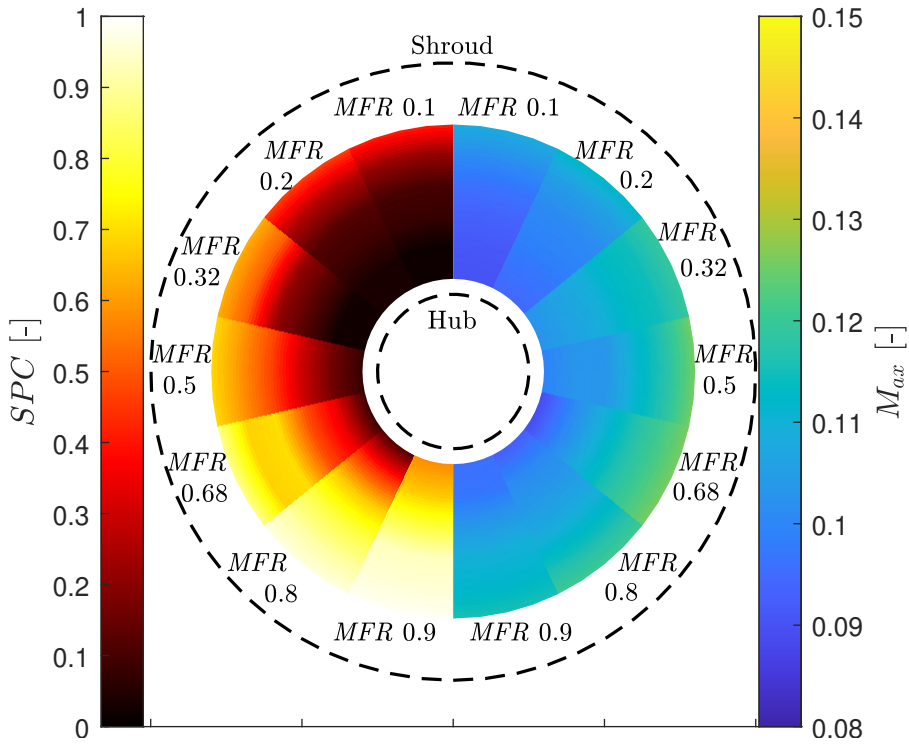

Figure 13. Shroud particle concentration (*SPC*) and axial Mach number for different *MFR* values.

Effect on the Area variation

The one-dimensional model presented in Galindo et al.[19] needs information about the rotor outlet area correspondent to each branch. In that work[19], a hypothesis of linear outlet area variation with the *MFR* value was made in the outlet effective area sub-model. This hypothesis was formulated based on CFD simulations results, but it could be corroborated with the current tests.

The rotor outlet area corresponding to each branch could be approximated using the *SPC* value. The position where the measurements have an *SPC* value of 0.5 could represent the limit between the rotor outlet region where there is mainly hub branch mass flow and where there is mainly shroud branch mass flow.

Fig. 14 shows the position where the *SPC* value is 0.5 for different *MFR* values. These positions have been obtained interpolating the results of the

measurement points. The whiskers indicate the variation with the reduced turbocharger speed. The extreme *MFR* values show small variations with the reduced turbocharger speed while the intermediate *MFR* values are practically independent of the reduced turbocharger speed.

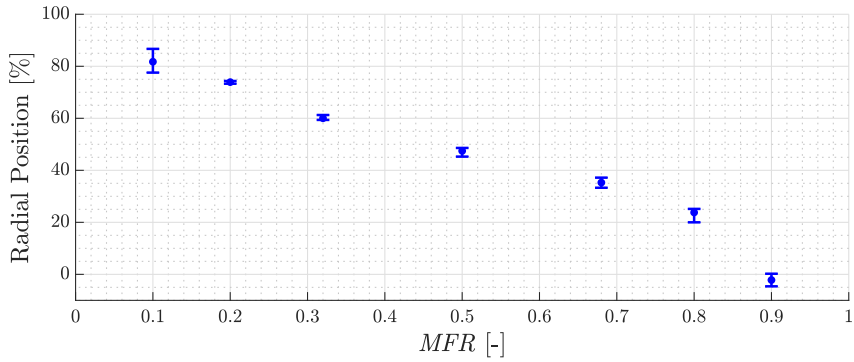

Figure 14. Radial position from hub to shroud where the *SPC* value is closer to 0.5 for different *MFR* values.

The position where the *SPC* value is 0.5, as shown in Fig. 14, goes toward the rotor hub when the *MFR* value increases, which is also observed in Fig. 13. Assuming these positions as a limit, the correspondent areas of each branch can be calculated, as shown in Fig. 15. Then, these areas can be compared with the CFD simulations results and the estimated area used in the one-dimensional model, shown in Fig. 1.

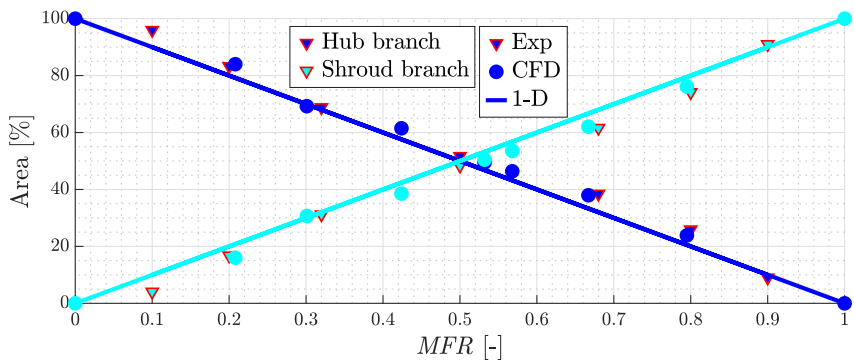

Figure 15. Outlet area corresponding to each flow branch for different *MFR* values.

The outlet area corresponding to each branch obtained experimentally has linear trends with the *MFR* value. The experimental results agree with

the CFD simulations results, as shown in Fig. 15. The CFD results were globally validated in previous works [19,20]. However, they have been locally validated in the outlet section now with these experimental measurements.

Moreover, these results corroborate the hypothesis of linear outlet area variation with the *MFR* value made in the one-dimensional model used [19]. Thus, the sub-model of outlet effective area used has been validated with the current work.

Conclusions

This paper presents an experimental assessment of the rotor outlet flow in a twin-entry radial turbine by means of LDA measurements.

The experimental results at the outlet section show the flow coming from each branch can be still differentiated despite the section is 13 mm downstream of the rotor. The region near the pipe wall has more concentration of flow coming from the shroud branch, and the region near the nut has more concentration of flow coming from the hub branch. This flow behaviour, in which both flow branches do not fully mix within the rotor, corroborates what was previously observed in the CFD simulations. So, the hypothesis of studying twin-entry turbines as two separated single-entry turbines has been corroborated.

The variation of the rotor outlet area corresponding to each flow branch with the *MFR* value has been studied, showing linear trends. These results match with the CFD results previously obtained. Thus, the hypothesis of linear outlet area variation with the *MFR* value that was used for developing the effective area one-dimensional model [19] has also been corroborated using LDA measurements.

The measured area has a small dependence on the reduced turbocharger speed for extreme *MFR* values. This effect has not been taken into account in the one-dimensional model. However, it is small enough to neglect it and even so provide a reliable model.

Declaration of Competing Interest

None declared.

Acknowledgement

The authors wish to thank V. Ucedo, R. Carrascosa and V. Samala for his invaluable work during the experimental setup and campaign.

Funding

Nicolás Medina is partially supported through contract FPU17/02803 of Programa de Formación de Profesorado Universitario of Spanish Ministerio de Ciencia, Innovación y Universidades.

Nomenclature

Abbreviations

1-D	One-dimensional
CFD	Computational fluid dynamics
EGR	Exhaust gas recirculation
ICE	Internal combustion engine
LDA	Laser Doppler anemometry
MFR	Mass flow ratio
ORC	Organic Rankine cycle
RMSE	Root mean square error
SPC	Shroud particle concentration

Roman letters

A	Area
a	Rotor discharge coefficient
b	Mass flow capacity fitting coefficient
c	Mass flow capacity fitting coefficient
d	Mass flow capacity fitting coefficient
D	Diameter
M	Mach number
$\dot{m}$	Mass flow rate
N	Turbocharger speed
n	Number
u	Uncertainty
u	Blade tip speed
v	Absolute velocity

w	Relative velocity

Greek letters

α	Absolute velocity angle
β	Relative velocity angle
γ	Specific heat capacities ratio
η	Efficiency
π	Pressure ratio
ρ	Density
σ	Blade to jet speed ratio

Subscripts and superscripts

2	Interspace outlet section
3	Rotor inlet station
4	Rotor outlet station
ax	Axial
exp	Expansion
geom	Geometrical
h	Hub branch
M	Mach number
Neq	Equivalent nozzle
red	Reduced
s	Shroud branch
samples	Samples
t	Turbulent
t, s	Total to static

Appendix A: 1D model

The one-dimensional model used is based on actuator disks for introducing the enthalpy and the momentum source terms. These source terms depend on the turbine operating point. The behaviour of the maps can be represented in terms of flow capacity and efficiency, but these paper has focused on the performance map in terms of flow capacity.

The one-dimensional model calculates the turbine flow capacity performance as an equivalent nozzle characterized by an effective area and dependent on the relative velocity w, the blade tip speed u, the absolute velocity in this equivalent nozzle, v and the ratios of areas and densities

between the rotor inlet and the rotor outlet sections, as shown in Eq. 4. The numerical subscripts are referred to the corresponding stage and the subscript Neq is referred to the equivalent nozzle. The volute inlet is defined as stage 0, the volute outlet/interspace inlet is defined as stage 1, the interspace outlet is defined as stage 2, the rotor inlet is defined as stage 3 and the rotor outlet is defined as stage 4.

$$A_{Neq} = A_4 \sqrt{\frac{1 + \left(\frac{u_4}{v_{Neq}}\right)^2 - \left(\frac{u_3}{v_{Neq}}\right)^2 + \left(\frac{w_3}{v_{Neq}}\right)^2}{\left(\frac{A_4}{A_3}\right)^2 \left(\frac{\rho_4}{\rho_3}\right)^2 + 1}} \tag{4}$$

Some of the variables in Eq 4 are difficult to measure properly even in the design operational points. Thus, some simplifications are used for modelling the effective area, as detailed in Serrano et al.[30]. So, the Eq. 5 depends only on the blade speed ratio σ, some pressures $\pi_{2,4}$, geometrical parameters as areas A, blade angles α and diameters D and 4 calibration coefficients a, b, c and d.

$$A_{Neq} = \frac{a \cdot A_4^{\text{geom}} \sqrt{1 + \frac{\sigma^2 \cdot \left[\left(\frac{D_4}{D_3}\right)^2 - 1\right] + b}{\eta_{\text{t,s}}}}}{\sqrt{1 + \left[c \cdot \frac{A_4^{\text{geom}}}{A_3^{\text{geom}} \cdot cos(\alpha_3)}\right]^2 \cdot \frac{\pi_{2,4}^{-2}}{\left[1 - \eta_{\text{t,s}} \cdot \left(1 - \pi_{2,4}^{\frac{1-\gamma}{\gamma}}\right)\right]^2}}} \tag{5}$$

a is the rotor discharge coefficient, b is the ratio between the rotor inlet relative kinetic energy and the nozzle isentropic kinetic energy, c is the ratio between rotor outlet and rotor inlet discharge coefficients and d is included through the term $\pi_{2,4} = 1 + d\,[\pi_{0t,4} - 1]$, being $d = (p_2 - p_4)/(p_{0t} - p_4)$. These four coefficients are set with available measured data.

Appendix B: CFD simulations

The CFD simulations are carried out with a non-structured polyhedral mesh with prism layer mesher near the walls. The regions with more complex phenomena arise have a more refined mesh. After a mesh independence study, as detailed in Galindo et al.[20], a 5.5 million cells mesh is chosen, as shown in Fig. 16. The global convergence index is less than 0.1% for the total pressure at the rotor inlet, the efficiency, the torque and the reduced mass flow. The method employed for calculating it is described by Roache[37] and this results match the required precision.

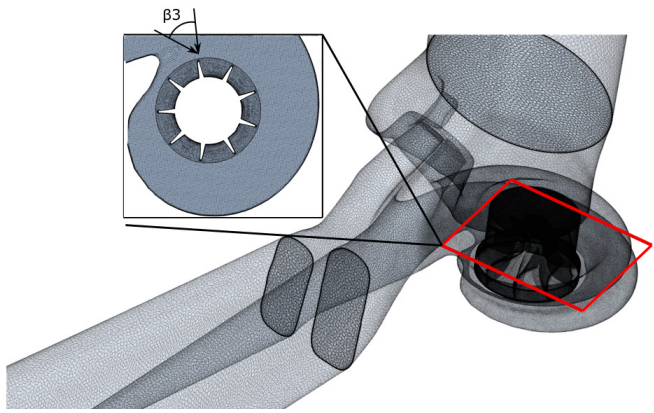

(a) General view of the mesh.

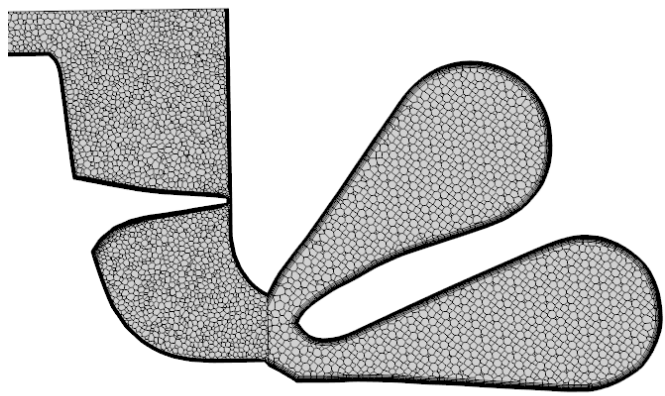

(b) Zoom at rotor and volutes mesh.

Figure 16. CAD model with final mesh.

The software used for simulating the geometry is the commercial software package Simcenter STAR-CCM+. The turbulence is modelled with the unsteady Reynolds Averaged Navier-Stokes (URANS) method. The turbulence model chosen is $k-\omega$ SST with compressibility correction and Durbin scale limiter for realizability. The equations are solved with an implicit, second order, upwind, coupled flow solver, using a Roe's flux-difference splitting scheme with Weiss-Smith preconditioning for all-speed flows.

Air is used as the working fluid and it is computed as an ideal gas with temperature-dependent specific heat capacity and dynamic viscosity. The air passing through each turbine entry is differentiated as hub air and shroud air respectively. Both fluids have the same exact gas properties, but the software allows the advection of these flows and tracking the concentration of each one locally using the passive scalar option. Therefore, the concentration of air coming from each branch can be followed along the geometry.

There are three boundary conditions with fixed values: a boundary condition for each turbine entry defined as stagnation inlets where the total pressure, total temperature, turbulence description and gas composition are fixed and a boundary condition for the turbine outlet defined as a pressure outlet, where the static pressure, static temperature, turbulence description and gas composition are fixed. Furthermore, the rotational speed of the rotor is also imposed ans set equal to that obtained from the experimental campaign.

First, the simulations are calculated fixing the geometry and using a moving reference frame for defining the rotor motion with a steady solver (RANS). These calculations lead to a more realistic initial conditions for the unsteady solver. When the steady solution is converged, the solver is changed to an implicit unsteady solver (URANS) and the motion is defined using a rigid body motion. In this case, the rotor mesh rotates each time step of the simulation while the volutes and outlet duct meshes are fixed. The time step used is constant and defined for each simulation as the time spent by the wheel in rotating one degree. Moreover, the simulations make twenty inner iterations for each time step in order to ensure the convergence of the results.

The simulations have been globally validated with experimental results. The comparison of both experimental and computational results of

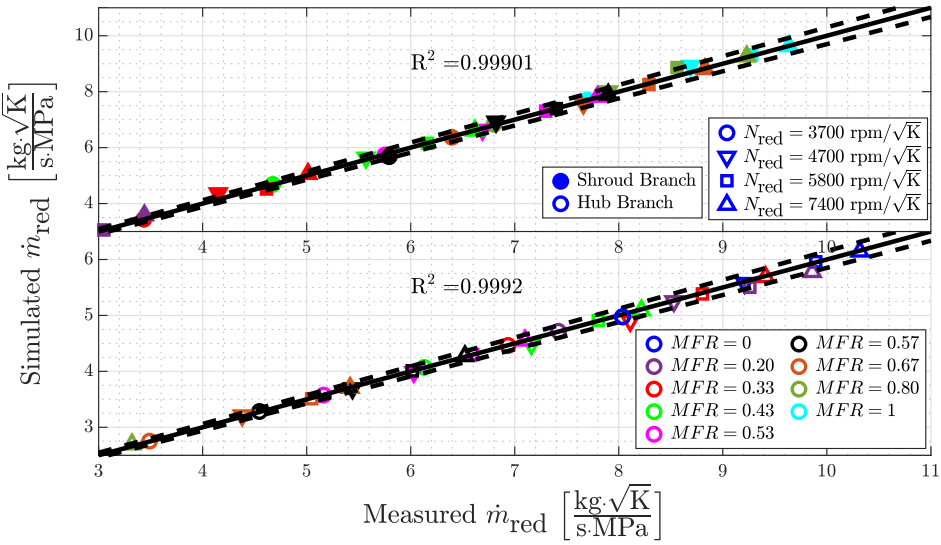

Figure 17. Validation of computational simulations with experimental results.

reduced mass flow rate for the mass flow capacity map has an error lower than 3% as shown in Fig. 17.

References

1. Yamamoto T, Furuhata T, Arai N et al. Design and testing of the Organic Rankine Cycle. *Energy* 2001; 26: 239–251. DOI:10.1016/S0360-5442(00)00063-3.
2. Facchinetti E, Favrat D and Marechal F. Design and optimization of an innovative solid oxide fuel cell-gas turbine hybrid cycle for small scale distributed generation. *Fuell Cells* 2014; 14: 595–606. DOI:10.1002/fuce.201300196.
3. Carlucci AP, Ficarella A, Laforgia D et al. Supercharging system behavior for high altitude operation of an aircraft 2-stroke diesel engine. *Energy Conversion and Management* 2015; 101: 470–480. DOI:10.1016/j.enconman.2015.06.009.
4. European Comission. Emissions in the automotive sector, 2018. URL https://ec.europa.eu/growth/sectors/automotive/environment-protection/emissions_en.
5. European Environment Agency. EEA Report No 13/2019, EMEP/EEA air pollutant emission inventory guidebook 2019, 2019. DOI:10.2800/293657.
6. Fraser N, Blaxill H, Lumsden G et al. Challenges for increased efficiency through gasoline engine downsizing. *SAE International Journal of Engines* 2009; 2: 991–1008. DOI: 10.4271/2009-01-1053.
7. Garrett T, Newton K and Steeds W. Turbocharging and supercharging. *Motor Vehicle* 2000; : 556–589.

8. Zhu D, Sun Z and Zheng X. Turbocharging strategy among variable geometry turbine, two-stage turbine, and asymmetric two-scroll turbine for energy and emission in diesel engines. *Proceedings of the Institution of Mechanical Engineers, Part A: Journal of Power and Energy* 2020; 234: 900–914. DOI:10.1177/0957650919891355.
9. Aghaali H and Hajilouy-Benisi A. Experimental and theoretical investigation of twin-entry radial inflow gas turbine with unsymmetrical volute under full and partial admission conditions. In *Turbo Expo: Power for Land, Sea and Air*. ASME, pp. 1099–1107. DOI: 10.1115/GT2007-27807. Paper No: GT2007-27807.
10. Brinkert N, Sumser S, Weber S et al. Understanding the twin scroll turbine: flow similarity. *Journal of Turbomachinery* 2013; 135: 021039. DOI:10.1115/1.4006607.
11. Cerdoun M and Ghenaiet A. Unsteady behaviour of a twin entry radial turbine under engine like inlet flow conditions. *Applied Thermal Engineering* 2018; 130: 93–111. DOI: 10.1016/j.applthermaleng.2017.11.001.
12. Menaouar BM, Mohamed H, Mohamed B et al. The separation wall effect of a volute twin entry cross section area on the mixed inflow turbine performance. *Engineering Review* 2020; 41: 11–20. DOI:10.30765/er.1383.
13. Liu Z, Romagnoli A, Palenschat T et al. Performance improvement of an asymmetric twin scroll turbocharger turbine through secondary flow injection. *SAE Technical Paper* 2020; DOI:10.4271/2020-01-1011.
14. Cravero A and Ottonello A. Uncertainty quantification methodologies applied to the rotor tip clearance effect in a twin scroll radial turbine. *Fluids* 2020; 5. DOI:10.3390/fluids5030114.
15. Jin J, Pan J, Lu Z et al. An investigation on performance of an asymmetric twin-scroll turbine with a small scroll bypass wastegate for a heavy-duty diesel engine. *Journal of Engineering for Gas Turbines and Power* 2020; 142. DOI:10.1115/1.4047123.
16. Jin J, Pan J, Lu Z et al. Effect of balance valve on an asymmetric twin-scroll turbine for heavy-duty diesel engine. *International Journal of Engine Research* 2020; DOI:10.1177/1468087420930162.
17. Wei J, Xue Y, Deng K et al. A direct comparison of unsteady influence of turbine with twin-entry and single-entry scroll on performance of internal combustion engine. *Energy* 2020; 212: 93–111. DOI:10.1016/j.energy.2020.118638.
18. Xue Y, Yang M, Martinez-Botas RF et al. Loss analysis of a mix-flow turbine with nozzled twin-entry volute at different admissions. *Energy* 2019; 166: 775–788. DOI:10.1016/j.energy.2018.10.075.
19. Galindo J, Serrano JR, García-Cuevas LM et al. Using a CFD analysis of the flow capacity in a twin-entry turbine to develop a simplified physics-based model. *Aerospace Science and Technology* 2021; 112. DOI:10.1016/j.ast.2021.106623.
20. Galindo J, Serrano JR, García-Cuevas LM et al. Twin-entry turbine losses: an analysis using CFD data. *International Journal of Engine Research* 2021; DOI:10.1177/14680874211007647.
21. Bornschlegel S, Conrad C, Durst A et al. The influence of superheated injection on liquid and gaseous flow field of an experimental single-hole gasoline direct injection injector. *International Journal of Engine Research* 2021; 22: 592–605. DOI:10.1177/1468087419858464.

22. Kumar A, Ghobadian A and Nouri J. Numerical simulation and experimental validation of cavitating flow in a multi-hole diesel fuel injector. *International Journal of Engine Research* 2021; Online First. DOI:10.1177/1468087421998631.
23. Theile M, Reißig M, Hassel E et al. Numerical analysis of the influence of early fuel injection on charge motion in a direct injection spark ignition engine using scale-resolving simulations. *International Journal of Engine Research* 2020; 21: 664–682. DOI:10.1177/1468087419860725.
24. Grosjean N, Graftieaux L, Michard M et al. Combining LDA and PIV for turbulence measurements in unsteady swirling flows. *Measurement Science and Technology* 1997; 8(12). DOI:10.1088/0957-0233/8/12/015.
25. Fischer A. Fundamental flow measurement capabilities of optical Doppler and time-of-flight principles. *Experiments in Fluids* 2021; 62. DOI:10.1007/s00348-020-03127-x.
26. Pedersen N, Larsen PS and Jacobsen CB. Flow in a centrifugal pump impeller at design and off-design conditions - Part I: Particle Image Velocimetry (PIV) and Laser Doppler Velocimetry (LDV) measurements. *Journal of Fluids Engineering* 2003; 125: 61–72. DOI:10.1115/1.1524585.
27. Theis A, Reviol T and Böhle M. Analysis of the losses in an axial fan with small blade aspect ratios using CFD-technique and laser Doppler anemometry. *Proceedings of the ASME Turbo Expo 2020: Turbomachinery Technical Conference and Exposition Volume 2A: Turbomachinery* 2020; DOI:10.1115/GT2020-14283.
28. Zhang N, Zheng F, Liu X et al. Unsteady flow fluctuations in a centrifugal pump measured by laser Doppler anemometry and pressure pulsation. *Physics of Fluids* 2020; 32. DOI:10.1063/5.0029124.
29. Galindo J, Serrano JR, Garcia-Cuevas LM et al. Experimental and computational analysis of the flow passing through each branch of a twin-entry turbine. *14th International Conference on Turbochargers and Turbocharging* 2020; .
30. Serrano JR, Arnau FJ, Garcia-Cuevas LM et al. Development and validation of a radial turbine efficiency and mass flow model at design and off-design conditions. *Energy Conversion and Management* 2016; 128: 281–293. DOI:10.1016/j.enconman.2016.09.032.
31. Serrano JR, Arnau FJ, Garcia-Cuevas LM et al. An innovative losses model for efficiency map fitting of vaneless and variable vaned radial turbines extrapolating towards extreme off-design conditions. *Energy* 2019; 180: 626–639. DOI:10.1016/j.energy.2019.05.062.
32. Galindo J, Tiseira A, Fajardo P et al. Development and validation of a radial variable geometry turbine model for transient pulsating flow applications. *Energy Conversion and Management* 2014; 85: 190–203. DOI:10.1016/j.enconman.2014.05.072.
33. Serrano JR, Arnau FJ, Garcia-Cuevas LM et al. Experimental approach for the characterization and performance analysis of twin entry radial-inflow turbines in a gas stand and with different flow admission conditions. *Applied Thermal Engineering* 2019; 159. DOI:10.1016/j.applthermaleng.2019.113737.
34. Serrano JR, Arnau FJ, García-Cuevas LM et al. An experimental method to test twin and double entry automotive turbines in realistic engine pulse conditions. *SAE Technical Paper* 2019; DOI:10.4271/2019-01-0319.
35. Serrano JR, Arnau FJ, García-Cuevas LM et al. Experimental validation of a one-dimensional twin-entry radial turbine model under non-linear pulse conditions. *International Journal of*

Engine Research 2021; 22: 390–406. DOI:10.1177/1468087419869157.

36. Olmeda P, Tiseira A, Dolz V et al. Uncertainties in power computations in a turbocharger test bench. *Measurement: Journal of the International Measurement Confederation* 2015; 59: 363–371. DOI:10.1016/j.measurement.2014.09.055.
37. Roache PJ. Perspective: A method for uniform reporting of grid refinement studies. *Journal of Fluids Engineering* 1994; 116(3): 405–413. DOI:10.1115/1.2910291.